

Developing an ML-based model for RF tuning of the DTL machine at ESS

Amin Hosseini Nejad



LUND
UNIVERSITY

Department of Automatic Control

MSc Thesis
TFRT-6193
ISSN 0280-5316

Department of Automatic Control
Lund University
Box 118
SE-221 00 LUND
Sweden

© 2023 Amin Hosseini Nejad. All rights reserved.
Printed in Sweden by Tryckeriet i E-huset
Lund 2023

Abstract

The European Spallation Source (ESS) infrastructure is being constructed in Lund, and will be one of the most powerful research facilities of its type in the world. The ESS linear accelerator (linac) utilizes different accelerating sections where a wide variety of techniques should be employed to accelerate a beam of protons to 2 GeV kinetic energy through Radio Frequency (RF) cavities before being collided with a tungsten target for the final production of neutrons, through the process of spallation.

This master's thesis is a continuation on another master's thesis project, (Lundquist, 2022), in which the focus was more on particle accelerator physics and to introduce some ML models using single-shot measurement scenario, which all failed to meet the requirements. This thesis, however, is focused on developing more ANN- models for both single-shot and multi-shot measurement scenarios, which succeed in meeting the requirements. Another focus of the project is to make the models small and feasible to be deployed in the ESS control system. The data is the simulated response of the Beam Position Monitor (BPM) sensors for the first Drift Tube Linas (DTL) tank, DTL1, at EES. DTL tanks are of great importance due to their influence on the overall performance. This will give the ESS physicists a powerful tool to direct the proton beam within the whole set of the DTL tanks properly, leading to a better control and thus, fewer beam losses once they start with the power ramp-up of the linac. The deployment of ML-based models in the ESS control system will be a step towards more automated and intelligent particle accelerators in this infrastructure and in similar future facilities.

Acknowledgements

I would like to thank Bo Bernhardsson and Johan Grönqvist at Department of Automatic Control at LTH. Thank you for being available in your office when I have had questions. Without your inputs, this project would have been significantly harder. Thanks to my ESS supervisors, Natalia Milas and Karin Rathsman, for supporting me with everything I needed at ESS, even in late hours and weekends. Thanks to Mamad Eshraqi at ESS for making me feel welcome in the group. Thanks to my wife, Sahar, and my daughter, Nika, for being patient and supportive during the whole master's program, especially the master's thesis.

I am also grateful for the offer of computational resources made available to the project by the National Academic Infrastructure for Supercomputing in Sweden (NAISS) and the Swedish National Infrastructure for Computing (SNIC) at Chalmers Centre for Computational Science and Engineering (C3SE), High Performance Computing Center North (HPC2N) and Uppsala Multidisciplinary Center for Advanced Computational Science (UPPMAX) partially funded by the Swedish Research Council through grant agreements no. 2022-06725 and no. 2018-05973.

CONTENTS

1	Introduction	9
2	Particle Accelerators	11
2.1	<i>Linear particle accelerators</i>	11
2.2	<i>The ESS Linac</i>	13
2.3	<i>Longitudinal Motion in Accelerators</i>	16
2.4	<i>RF Tuning</i>	18
2.5	<i>RF Phase Scan</i>	19
2.6	<i>General overview of the RF phase curves</i>	21
2.7	<i>Single-shot measurement concept</i>	23
2.8	<i>Machine Learning in modern accelerators</i>	24
2.9	<i>Problem Statement</i>	26
2.10	<i>Applications of modeling in DTL process</i>	27
3	Methodology	28
3.1	<i>Data handling</i>	28
3.1.1	<i>Data generation</i>	28
3.1.2	<i>Data investigation</i>	29
3.1.3	<i>Data pre-processing</i>	32
3.2	<i>ANN model weight initialization</i>	34
3.3	<i>ANN model weight scaling</i>	34
3.4	<i>ANN model description</i>	34
4	Measurement scenarios and Results	40
4.1	<i>Description of histogram plots</i>	40
4.2	<i>Single-shot measurement scenario</i>	42
4.3	<i>Double-shot measurement scenarios</i>	44

4.3.1	In RF phase direction	45
4.3.2	In RF amplitude direction	48
4.4	<i>Triple-shot measurement scenario</i>	51
5	Discussion and future work	57
6	Conclusion	60
7	Bibliography	61

FIGURES

Figure 1. Schematic model of pillbox cavities	12
Figure 2. Schematic of the cross-section of a BPM.	13
Figure 3. Simplified schematic of the ESS linac layout.....	14
Figure 4. The ESS linac tunnel and DTL tanks.....	15
Figure 5. A sinusoidal electric field with the particles.....	17
Figure 6. The phase curves for different tuning set-points.....	21
Figure 7. Non-function mapping between the inputs and the outputs.....	22
Figure 8. BPM phase differences using single-shot measurement.....	23
Figure 9. Distribution of the data related to the first feature	31
Figure 10. Correlation heat-map of the input data	32
Figure 11. ANN model structures	36
Figure 12. Laptop specifications	37
Figure 13. Training and validation losses versus epochs.	38
Figure 14. Number of mispredictions during training	39
Figure 15. Histogram of prediction error of single-shot measurement	43
Figure 16. Double-shot measurement in RF phase direction	45
Figure 17. Histogram of prediction error in RF phase direction.....	47
Figure 18. Double-shot measurement in RF amplitude direction.....	48
Figure 19. Histogram of prediction error in RF amplitude direction.....	50
Figure 20. Triple-shot measurement scenario	52
Figure 21. Histogram of prediction error for triple-shot measurement	54

TABLES

Table 1. Required prediction errors by ESS.....	26
Table 2. Different types of errors and their magnitudes.....	33
Table 3. Model structure and hyperparameter values	44
Table 4. Prediction accuracies for different RF phase shifts	46
Table 5. Prediction accuracies for different RF amplitude shifts	49
Table 6. Prediction accuracies for different phase and amplitude shifts	53
Table 7. Results summary	56

1 Introduction

The European Spallation Source (ESS) has a linear accelerator (linac) designed and is currently fabricated to accelerate a beam of protons with 62.5 mA, 2.86 ms long pulses, working at 14 Hz [1]. The final section of its normal-conducting cavity setting consists of a 39 m long drift tube linac (DTL) divided into five tanks, designed to accelerate the proton beam from 3.6 MeV to 90 MeV. The high beam current and power impose challenges to the design and tuning of the DTL machine. In order to keep the beam quality throughout the accelerator and to keep beam losses at minimum levels, the Radio Frequency (RF) amplitude and phase within the accelerating components have to be set within 1% and 1° of their design values in DTLs, respectively.

Machine learning (ML) has proven to be successful in many applications, accelerators are not an exception, but tuning of the RF fields in accelerators using such techniques and deploying resulting models in their control systems has yet to be tried. This project aims to apply ML techniques, focusing on ANN models, in the field of particle accelerator physics, resulting in new possibilities for much faster machine tuning. The first tank in the DTL section of the ESS linac, DTL 1, is the case study in this project. Since this part of the linac is still under pre-commissioning and commissioning, the real data of tuning set-points of the machine have not been provided yet. Thus, some data is simulated using OpenXAL [2], and some noise is added to the simulated data to make the models robust against any difference between the distribution of the simulated data and the future real data. Such data was then used to train ANN models to capture behavior of the data.

The physical properties of interest that we could observe in the machine are Beam Position Monitor (BPM) phase measurements in the tank, as the input data; while the ones we would like to predict by some ML models are the RF phase and amplitude, and the input energy of the proton beam into the cavity. There exist too many data samples whose

labels are almost the same while they are quite different. Hence, the simulated data here, we are not facing a function mapping between the inputs and outputs. That will be discussed in detail in 2.6, showing that single-shot measurement scenario does not work well for the data. Thus, some techniques like multi-shot measurement scenarios should be tried to see if any improvement with the prediction performance of the models could be made. That will be discussed more in 4.2.

The thesis will begin with a general introduction to the particle accelerators like the one at the ESS, and RF tuning methods in such infrastructures in chapter 2. Next, the methodology of the project consisting of different data handling steps are presented in chapter 3. Then, different measurement scenarios and the obtained results are presented in chapter 4. In chapter 5, the results are analyzed and discussed in details and some potential future work is suggested. Finally, in chapter 6, some conclusions are derived.

2 Particle Accelerators¹

To get familiar with the content and the scope of the project, some information on particle accelerators and ML applications in such systems are presented in this chapter. First, an overall description of linear particle accelerators and the ESS linac are provided in 2.1 and 2.2, respectively. Next, some explanations on physical processes in such systems and their stability characteristics are discussed in 2.3. RF tuning is explained in 2.4 and a common traditional technique to do it is presented in 2.5. Then, some details on RF phase scan curves are provided in 2.6, and the single-shot measurement concept is explained in 2.7. Lastly, the ML applications in particle accelerators are reviewed in 2.8, followed by the problem statement and modeling applications in the DTL process, which are presented in 2.9 and 2.10, respectively.

2.1 Linear particle accelerators

In very initial accelerators, some constant electric fields used to be generated to impose gradient forces to some charged particles, like electrons or protons, to accelerate them, but in order to reach high output energies, extremely high voltages are required, causing electric breakdowns at a few tens of megavolts. This has led to the application of RF fields, time-varying electric fields, in particle accelerators in such a way that it maintains a phase relative to the beam to ensure continuous acceleration as the field oscillates. These fields are housed within cavities, with some form of entrance and exit so the beam can move straight through while gaining energy from the fields in the gaps between the cavities. The particles velocity, described relative to the speed of light, as $\beta = \frac{v}{c}$, increases throughout the linac.

¹ In this chapter, the particle accelerator physics should be briefly introduced and discussed to give a clear picture of the project scope. Since the main focus in this project is on developing ML models, while in the previous master's thesis, [4], the main focus was on particle accelerator physics, some particle-physics concepts are borrowed from the previous master's thesis in this chapter.

The most basic form of the "RF structure" used in linacs is pillbox cavities, a cylindrical space with openings for entrance and exit. A schematic model of such cavity and the RF fields flowing within it can be seen in Figure 1.

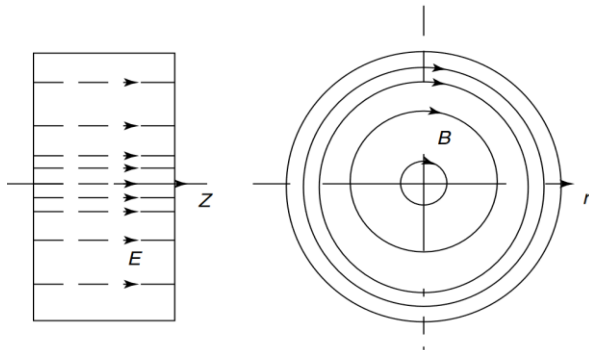


Figure 1. Schematic model of pillbox cavities, electric field (E) and magnetic field (B) components of an RF field. In proton accelerators like the one at EES, the beam moves along the z -direction [3]

Any type of charged particle could be accelerated in such machines, two most common ones are protons and electrons. Modern proton linacs, like the one at the ESS, are in many ways comparable to their electron counterparts. The RF fields are generated by the Low-Level RF (LLRF) system and amplified by the klystrons. The modulator is the power supply for the klystrons. Different design considerations should be taken into account to ensure that particles get exposed to only the accelerating part of such oscillating fields while travelling through the gaps, and not being decelerated.

The components which help to understand and diagnose the beam are called diagnostics. Perhaps the most important and commonly used diagnostic elements in particle accelerators are the Beam Position Monitor (BPM) sensors, consisting of four electrodes and assembled on the walls of the vacuum chamber housing the beam. As the beam passes by a BPM, both the amplitude and phase of the fields generated in the BPM electrodes are

read out. Although such a BPM phase alone does not hold much information, by comparing two BPM phases, we can get a fast measurement which is proportional to the time-of-flight, or from the acceleration perspective in RF cavities, the energy gains between two neighboring drift tubes. It is important to mention that this measurement is relative and extracting the absolute values of the energy is not an easy task. For this project, however, using only the fractional phase changes is proven to be enough. Since BPMs are indirect sensors to energy, they are useful diagnostics to use during RF tuning. A simple schematic of the longitudinal and transverse cross-sections of a BPM can be seen in Figure 2.

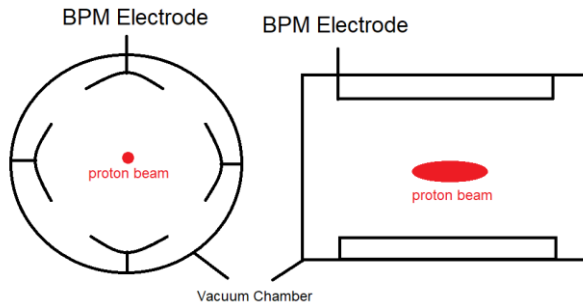


Figure 2. Schematic of the cross-section of a BPM, with longitudinal and transverse cross-sections, on the left and right respectively [4].

2.2 The ESS Linac

In Figure 3, a simplified model of the linac at ESS is presented. There are two main goals for the linac design: final average beam power to reach 5MW, and final beam energy being 357 kJ. Preserving the goals, the linac has been designed with 9 separate sections. 5 of the sections are accelerating ones contributing to final energy of the protons, 2 GeV on the tungsten target, while the rest make bunches of the beam while traveling through the linac.

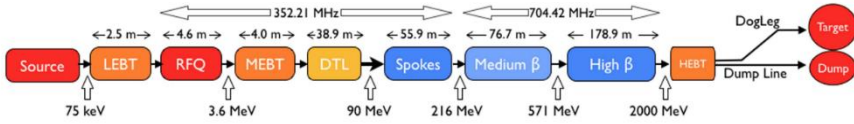


Figure 3. Simplified schematic of the ESS linac layout [5].

The protons are generated by a microwave-discharge ion source, designed to output a continuous beam with an energy of 75 keV. The particles then travel to the Low Energy Beam Transport (LEBT) section, which includes multiple diagnostics, magnetic focusing elements and a chopper that shapes the beam to the nominal 2.86 ms long pulse required in the later sections. The next element is the Radio-Frequency Quadrupole (RFQ). This is a RF structure, operating at a fundamental frequency of 352.21 MHz, which is designed to bunch, accelerate and focus the beam all at once. After this acceleration, the beam has reached the 3.6 MeV and enters the Medium Energy Beam Transport (MEBT) section. This serves a similar functionality to the LEBT, but also includes three buncher cavities to improve the beam input in the longitudinal plane to the following section. The Drift Tube Linac (DTL) then covers the next 40 m of the linac, shown in

Figure 4, raising the energy of the beam to 90 MeV, using the same frequency as the RFQ section. The first of these superconducting structures after DTL are the spoke cavities, 13 separate cryo-modules containing two spoke cavities each, which raise the proton energy to 216 MeV. After the spokes, the beam will travel through the medium and high β sections, consisting of 9 and 21 cryo-modules respectively, each housing 4 cavities. These two last accelerating sections, operating at twice the RF frequency of previous ones, raise the beam energy to the final design value of 2 GeV. After there are 2 separate transport lines, which guide the beam to either a final beam dump if it is not to be used for neutron production, or through the DogLeg and Accelerator-to-Target (A2T) sections, to finally impact on the tungsten target to produce neutrons for the experimental stations [5].

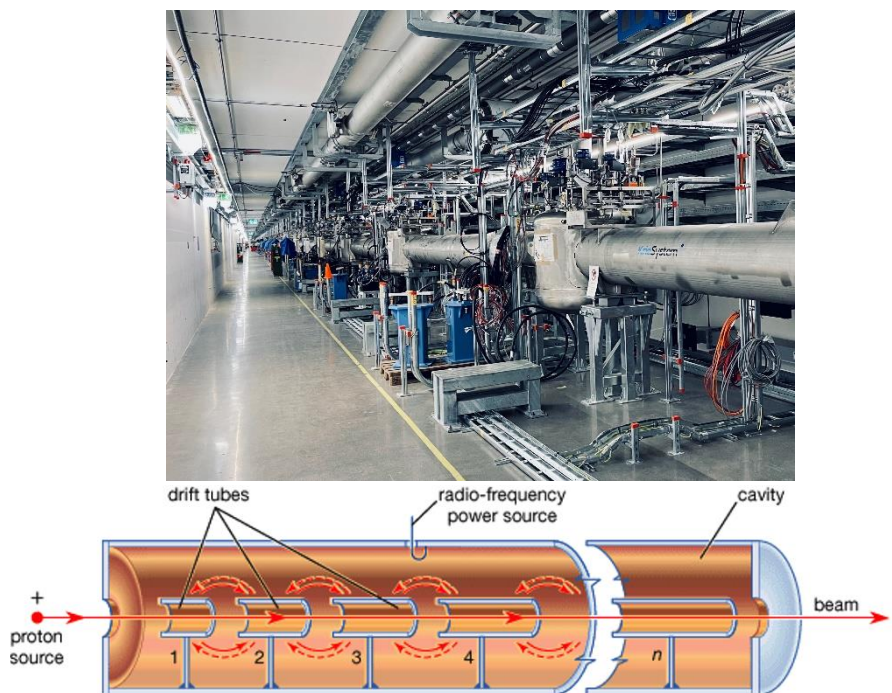


Figure 4. The ESS linac tunnel (top) [6], schematic of DTL tanks (middle) in which radio-frequency power source settings are RF phase and RF amplitude [7], drift tubes in a DTL tank (below left) [8], and the ESS DTL1 tank assembled (below right) [9], with the BPM sensors on the top of the tank inside the green covers in the photo

2.3 Longitudinal Motion in Accelerators

As batches of particles travel through the cavity, they maintain a certain spread around a central particle, called the synchronous particle, being synchronous relative to the accelerating time-varying fields. It always arrives to the cavity when the field inside is the design amplitude while moving from gap to gap in the accelerating field, thus it experiences the ideal acceleration. This is the particle which a linac structure is based on designed. Particles will not have to be synchronous to remain stable and at the same time, to be accelerated. This is due to what called longitudinal phase stability.

In proton linacs, by keeping the time relation between incoming particles of a travelling batch and the RF fields in a way that the particles arrive upon the rising or falling parts of the fields, a focusing effect in time can be achieved. This is demonstrated for proton particles in Figure 5. This is somehow intuitive by considering a batch of particles moving through a series of accelerating gaps. The synchronous particle could arrive on either the rising part or the falling part of the RF field as it moves through the gaps, while the particles having less energies will arrive later since they have lower velocities as well. This leads to such particles facing the low-amplitude part of the time-altering field if the synchronous particle arrives in the falling part of the field or vice versa if it does in the rising part; hence, they will gain higher energies or lower energies than what they had in the previous gap depending on the part of the RF field where the synchronous particle arrives upon. Gaining more energy by such late particles is desired to avoid them from getting lost; hence, we want the synchronous particle to arrive on rising part to make the movement of the late particles stable. In addition, in the subsequent gap, the previously-late particles will arrive earlier, due to their higher energies compared to the synchronous particle, and will gain lower energies from the RF field due to being already high energy. Thus, such particles oscillate around the synchronous particle provided that it arrives on the rising part of the field. A similar logic can be used for particles having more energy than the synchronous particle. They need to get low energies from the RF field not to get separated from the synchronous particle and the batch; hence, for such particles in the

batch, it is more desirable to have the synchronous particle arrived in the rising part. This phenomenon introduces two fixed points on the RF waves: the first is stable and the second is unstable. As can be seen in the middle plot in Figure 5, the particles of a batch oscillate around the synchronous particle while the batch travel along gaps if the synchronous particle arrives on the rising part of the RF field; otherwise, the batch falls apart and the particles get out of the batch.

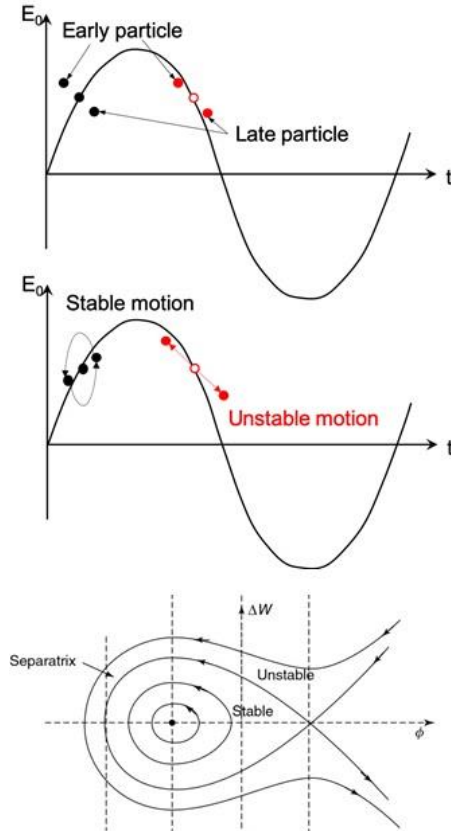


Figure 5. A sinusoidal electric field with particles arriving at different times, and the separatrix, [4]

Longitudinal phase stability allows the beam a certain level of spreading in the longitudinal phase space while still gaining energy and remaining stable, but there are some specific limits in here. For a beam of protons, arriving on the falling part makes the batches unstable. The resulting limits of stability, which are calculated beyond the scope of this project, is often called *separatrix*, within which the stable region of the phase space is called the *bucket*. The separatrix and its bucket are shown in the below plot in Figure 5. Such a separatrix in DTL 1, relevant to scope of this project, shows the possibilities of setting the RF field parameters to tune the machine to generate stable beams. Accelerations through insufficiently or inaccurately tuned machines lead to some particles ending up outside the bucket, and thus eventually being lost.

2.4 RF Tuning

The ESS linac is a high-power accelerator and any losses will have long-lasting repercussions. Sudden losses of the proton beam may result in some damage to different parts of the machine caused by the dissipated power. These types of losses can be catastrophic, but they are often avoided using machine protection systems not covered by this project. The losses relevant to the work of RF tuning are slow, coming from inefficient acceleration or mismatched optics, which can result in activating the surrounding components undesirably, limiting any access to the linac elements and machinery being necessary for ongoing operations or maintenance and subsequently, delays in operation. Such slow losses can be minimized by ensuring that the acceleration is optimized by proper tuning of the accelerating RF fields.

The RF fields within the accelerating cavities are generated by a klystron connected to an RF modulator. The exact field amplitude and phase experienced by the passing beam does not correspond exactly to the one set by the klystron control since the true magnitudes depend on losses in the wave guides and construction tolerances of the resonant structure the klystron is connected to. The following sections describe the most

common methods for determining the actual RF phase and amplitude experienced by the beam.

2.5 RF Phase Scan

In order for the DTL tanks to have acceptable matching with the upstream sections of the ESS linac, the field in RF accelerating cavities must be set within 1% in amplitude and 1° off in phase of the design set-points; thus, an accurate technique is needed to fulfill the requirements. In order to specify how the beam responds to changes with the RF set-points, some diagnostics that are sensitive to the beam time of flight within the cavity, should be used. In such cases, Beam Position Monitors (BPM) can serve the purpose.

As the most common RF phase scan method, a cavity is set with a certain value of RF amplitude while the RF phase is scanned through its full range. This scan is repeated for different values of RF amplitude inside the cavity, and then, the predictions using some simulation-based models, like signature matching technique in [4], are compared with the data collected here. Based on such iterative comparison, the proper RF phase and RF amplitude are specified so that they get in line with their corresponding design values. Two examples of such simulation data, similar to the RF phase scan data in reality, can be seen in Figure 6.

Such RF phase scanning is an established and reliable method for extracting the information needed to achieve good tuning, and having limited number of diagnostics, it is the only option available. However, having plenty of BPMs within the ESS DTL1 tank, an idea of a much faster alternative was proposed by [4], but the proposed models failed to meet the requirements. Hence in this project, the goal is to develop some ANN models which meet the requirements alongside being feasible and practical to be deployed as a tuning and monitoring tool in the ESS control system.

As the RF phase scan method is simulated using OpenXAL here, in addition to the RF amplitude, the cavity input energy could be another

physical property that plays a role. In reality, however, that is not possible, for there is no way to measure and set the cavity input energy in DTL tanks in practice. On the other hand, the BPM pair phase difference signals proportional to the beam time-of-flight, so the cavity input energy can be calculated using some techniques like in [10]. Hence, the presented models which are fitted to the BPM phase difference data could serve two goals; one as an RF tuning and monitoring tool, and another as a virtual diagnostics (sensors) tool for the cavity input energy if the predictions are of high accuracies.

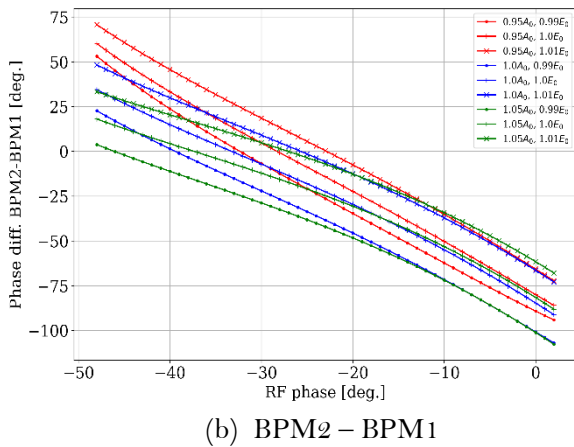
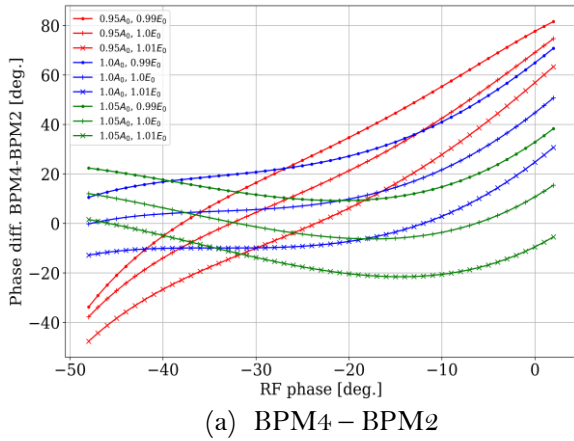


Figure 6. The phase curves for different tuning set-points related to two BPM pairs in the first DTL tank 1 in the ESS linac, [4]. A_0 and E_0 are designed values of the RF amplitude and input energy of the cavity in DTL1, respectively.

2.6 General overview of the RF phase curves

As an important investigation into the RF phase curves data to check how many quite different label points are mapped (correspond) to almost the same input points in the dataset, it turned out that there are lots of such

sample points that regardless of any model structures, they could raise confusion for models to predict the true labels. An example of such sample point is shown in Figure 7, where the orange line connects two black points of the same BMP pair phase differences, the same RF amplitudes and the same input energies, but totally different RF phases. If that happens for all the BPM pairs used in the dataset at the same time, any model gets confused on what the true RF phase is by looking at the BPM phase differences as the input. That is the case in our data; hence, we need at least two shots of measurements for the models to predict the true outputs correctly.

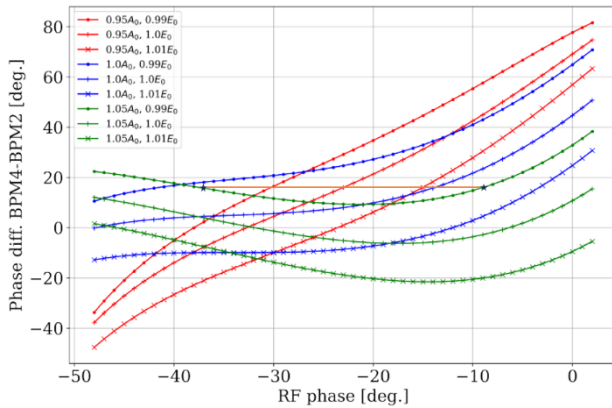


Figure 7. Non-function mapping between the inputs and the outputs of the dataset we have at ESS

There is some other behavior in the data that needs to be considered; it is not always easy to differentiate every curve from any others even for human beings, for example in RF amplitude direction in the plot (b) in Figure 6. As it can be seen, the curves of the same line styles, showing the same RF phases and input energy values but different RF amplitudes, overlap within the RF phase range of $[-15, 4]$ degrees. That would cause fundamental limitations in RF amplitude predictions using any models.

2.7 Single-shot measurement concept

As discussed in 2.5, the traditional RF phase scanning is a common and reliable method to extract the information needed to achieve good tuning. However, having plenty of BPMs within the ESS DTL tanks, a good reconstruction of the data can be done such that we can see distinct signatures for each cavity set-point in amplitude, phase and beam input energy without the need for a full phase scan. We look at BPM phase differences, not versus RF phase values, but versus each BPM pair. Figure 8 shows an example of such a plot, where each line represents a cavity set-point which is measured in a single-shot scenario through the machine.

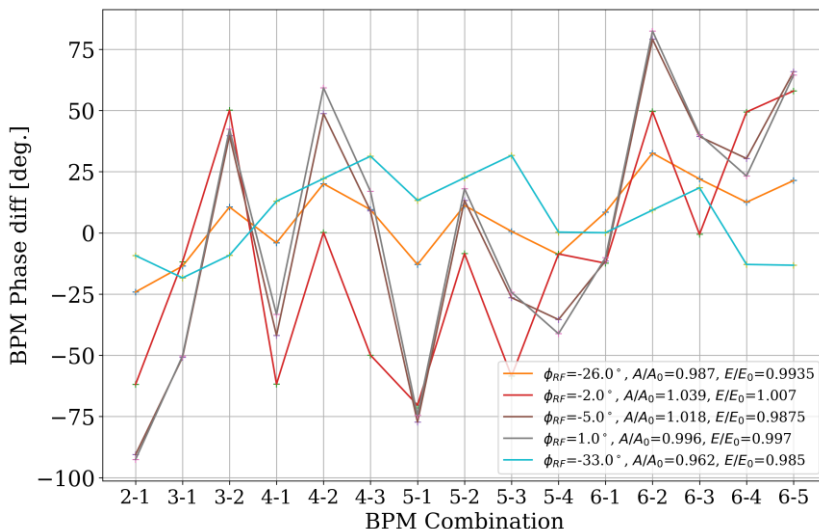


Figure 8. BPM phase differences for each possible BPM pair using single-shot measurement scenario; each curve corresponds to a cavity set-point, [4].

It should be noted that the phase difference values of BPM pairs are relative, meaning that, for example, the phase difference of the BPM3-BPM2 equals to the phase difference of the BPM3-BPM1 subtracted by the phase difference of the BPM2-BPM1. Hence, the phase differences of all the BPM pairs are not needed, but only the ones which are relative to the one

of the BPMs, that could be BPM1 which is the most reliable and accurate one, are needed to create the dataset. That would result in a smaller number of features which are uncorrelated, which could make the models avoid overfitting. That is the dataset available to develop the ANN models based on.

If good models could be developed, there will be some advantages in tuning the RF field of the DTL section in the ESS linac. Being able to tune the machine acceptably through a single shot or a few shots could cut down the time needed to tune and run the machine substantially. One would also not need to determine a good range for the parameters through scanning techniques as in more traditional RF tuning [11], but would in principle just need to reload the last machine state with good settings and run a single or a few verification pulses to calibrate the models with real distribution of data. Another application of accurate models could be virtual diagnostics for the signal which are hard to measure, like the cavity input energy in the ESS DTL tanks.

2.8 Machine Learning in modern accelerators

Particle accelerators are some of the largest, most data-intensive, and most complex scientific infrastructures in existence. The interrelations between machine subsystems are complicated and often nonlinear, the system dynamics involve large parameter spaces that evolve over multiple relevant time scales, and accelerator systems can be difficult to model *a priori*. Relevant problems for accelerators include, for example, analysis of large quantities of archived data, accurate and fast modeling of accelerator systems, detection of aberrant machine behavior, optimization of accelerator design, and active tuning and control. At present, ML-based approaches are technologically mature enough to be brought to bear on a wide variety of problems within these domains.

ML techniques have been applied to particle accelerators since the late 1980s. Much early discussion during the late 1980s and early 1990s focused on applying rule-based systems to accelerator control and tuning, [12],

[13], and [14]. In the early 1990s, scientists at Los Alamos National Lab had some experimental success with neural-network-based ion source control, [15], [16], and [17]. Other early studies at the University of New Mexico focused on orbit/trajectory control, [18] and [19] and fault detection and management [20]. General AI/ML platform for beamline tuning were also planned [21]. None of these systems were eventually used routinely as part of an accelerator's main control system. The lack of clear success in bringing ML to regular use in accelerator systems was partly due to limitations in the then-available hardware, algorithms, and software packages, as well as the limited accessibility of good data sets and simulation tools. Similar situations were encountered in other scientific fields where ML approaches were tried before they had reached sufficient technological maturity relative to the challenges of the particular application.

Diagnostics, such as the BPMs employed for this project, are vital elements for tuning and running particle accelerator. They, like any other elements, can become non-functional, unreliable or faulty. There might be some construction limitations in accelerators which do not allow for diagnostics in needed areas. In all such cases, virtual diagnostics, where ML techniques could be employed to model the system to provide an estimate of what a diagnostic would read when such a reading is unavailable, could be a good idea. Some examples are the longitudinal phase space predictions from SLAC [22] and a virtual instrument developed at LANSCE [23].

The use of ML techniques to build models to do RF tuning and monitoring at the ESS DTL1 was tried in the previous master's thesis [4], but the models failed to meet the requirements. This project aims to gain better results using smaller, simpler, and faster models which could be deployed in the integrated control system at the ESS.

2.9 Problem Statement

In ESS DTL section, the requirement for prediction error of the RF setpoints must be at most within 1% and 1° off relative to their corresponding design values in amplitude and phase, respectively. The requirements are presented in Table 1. Since the range of unscaled original RF phase is $[-50,4]$ degrees, when they are scaled to the range $[0,1]$ degrees using *MinMaxScaler* Python function, the prediction error should be also scaled into the range; hence, the scaling factor of required prediction error bound for the scaled RF phase is $\frac{1}{4-(-50)} = \frac{1}{54}$ of the required prediction error bound for the original RF phase. The required prediction error bound for the input energy is considered to be 0.1% to figure out how accurate the models are. The range of the original input energy is $[0.99,1.01]$, resulting in $(\frac{1}{1.01-0.99} = \frac{1}{0.02} = 50)$ as the scaling factor of the prediction error bound for the scaled input energy with respect to the original input energy.

Output	Scaling factor of required prediction error bound for the scaled data with respect to the FSR data	Required prediction error bound for original or Full Scan-Range (FSR) data
RF phase	$\frac{1}{54}$	1 degree
RF amplitude	1	1%
Input energy	50	0.1%

Table 1. Required prediction errors by ESS; the required prediction error bounds for the data scaled into $[0,1]$ (the middle column) as a factor of the prediction errors for the FSR data (the left column)

Since this project is a continuation on the previous master’s thesis, in which only single-shot measurement scenario was implemented and the models did not meet the requirements, careful data handling and some other measurement scenarios should be performed to develop some models

which can meet the requirements. Being able to tune the machine properly using just a few shots, instead of the time-consuming RF phase scans, could cut down the set-up time noticeably since the total number of such RF stations at the ESS is in the order of 100. In addition, as there is no way to measure the cavity input energy in practice, neither in DTL section nor in the upstream sections, the models which can give an accurate indication of it to the beam physicists at the ESS are so helpful and practical.

2.10 Applications of modeling in DTL process

There are some applications which need the models to outperform the design requirements, while some others can still go with low-performance models. An example of such first applications is RF tuning of the DTL machine. After every major machine shutdown or anytime the RF system is altered, RF tuning should be performed. Models could be used to help the machine operators to start up or ramp up the machine properly in shortest time, so it is important to have high-performance models that could meet the design requirements. On the other hand, some examples of the latter applications are monitoring and verification. Verification is needed when a configuration of the machine is already loaded via RF tuning, and it needs to ensure that the model still works well on new real-time data. Monitoring is needed to keep track of the process within the machine in case of slow changes and drifts.

3 Methodology

In this chapter, the methodology used in the project is described in detail. It consists of the steps we need to take to handle the data and the measurement scenarios implemented in the project. Lastly, the results using the best models developed for different measurement scenarios are presented.

3.1 Data handling

The quality of training data has a huge impact on the efficiency, accuracy, and complexity of machine learning tasks. Neglecting or simply not going the extra mile to ensure that the quality of the data used is up to standards can adversely affect the entire machine learning process. Thus, it is so worthwhile to scrutinize the data before developing any models based on it. In this section, the data used in the project is defined in 3.1.1, investigated in 3.1.2, and lastly, pre-processed in 3.1.3 in detail. Subsequently, two helpful techniques to develop good ANN models, such as weight initialization and weight scaling, are presented in 3.2 and 3.3, respectively. Lastly, the ANN models presented are described in detail in 3.4.

3.1.1 Data generation

In this project, the process in the first DTL tank, DTL1, is simulated using the accelerator environment OpenXAL. It is an open-source software environment coded in Java for accelerator physics. It has been developed in a collaboration among many different accelerator facilities, ESS and The Spallation Neutron Source (SNS) among them.

Phase differences of the BPM pairs are the data of interest as the input in the dataset, while the RF amplitude, RF phase and input energy are the labels. As mentioned before, since there are high dependencies between the phase differences of the BPM pairs, just the ones relative to the first BPM,

BPM1, are considered as the input of the dataset. Artificial neural networks (ANN) make high prediction performance possible when big data is provided to train them. As the data used in this project are simulation data, there are no limitations in generating huge amounts of data. In this project, 110 different RF amplitude values, with a variation of $\pm 5.5\%$ around the design RF cavity amplitude $A_0 = 6.89$ MV, 60 different input energy values, with a variation of $\pm 1.5\%$ around the design input energy $E_0 = 3.6$ MeV, and 55 different RF phase values, spread evenly around -35° as the design value for RF phase is considered to simulate the data.

3.1.2 Data investigation

There are some common data investigation and data processing actions needed to be accounted for in all the scenarios, especially when working on real data. First, missing data points or outliers should be imputed or removed not to effect the performance of models negatively. As in this thesis, the data are simulated, there is no need for dealing with such problems. Plus, we need to check the distribution of the data to make sure if there is a need for any transformations, like log-transform to make the data more Gaussian and less skewed. The ANN models can handle little skewness in the data due to being nonlinear and their complexities especially in their hidden layers [24]; while if distribution of data is highly-skewed, it can reduce the performance of the model significantly. That can be checked by Box-Cox transformation technique [25]. Having each feature data in the project almost normally distributed, an example illustrated in Figure 9, there is no need for any transformation. In this figure, the left plots regard the original unscaled data, while the right ones relate to the scaled data; the top plots are for the training data, the middle ones for the validation data, and the below ones for the test data; showing that distribution of the training, validation and test datasets are almost the same, as they should be. Furthermore, drawing correlation heat-map of the input data, depicted in Figure 10, some high correlations between different features can be realized. Making the data less auto-correlated through only keeping the features that do not have so much correlations and removing

the others, we can perform some data reduction, resulting in more clean and useful data. It is useful to mention that $\text{BPM}_2 - \text{BPM}_1$, $\text{BPM}_3 - \text{BPM}_1$, $\text{BPM}_4 - \text{BPM}_1$, $\text{BPM}_5 - \text{BPM}_1$, and $\text{BPM}_6 - \text{BPM}_1$ phase differences are shown by features 0 to 4 in the heat-map plot. Regarding our data, it can be seen that the phase difference values of $\text{BPM}_2 - \text{BPM}_1$ and $\text{BPM}_4 - \text{BPM}_1$ are highly correlated, so we can exclude the $\text{BPM}_4 - \text{BPM}_1$ phase difference data from our dataset due to having real data of the other pair more reliable.

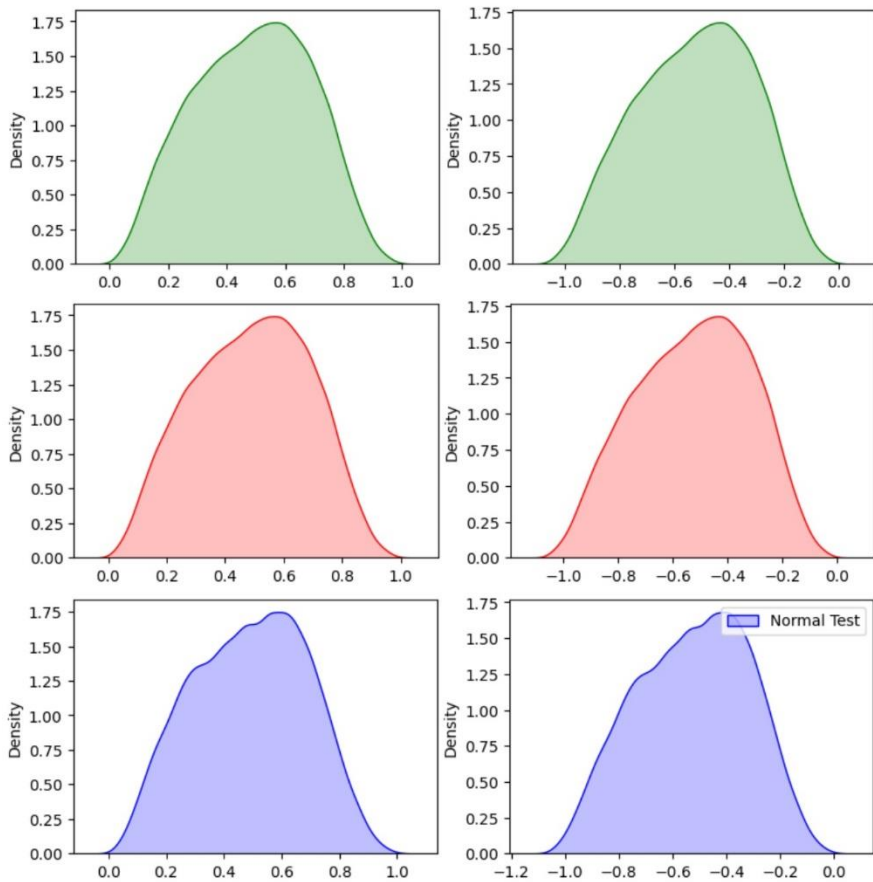


Figure 9. Distribution of the data related to the first feature (the BPM2-BPM1 phase difference); it is fairly Gaussian, so no need for any transformation. The lambda value in Box-Cox criterion for such data is 0.93, proving that linear transformation, or explicitly no transformation, is needed. The left plots regard the scaled data, while the right ones relate to the Box-Cox transformed data. Having similar distributions before and after the transformation proves that there is no need for transforming the data. The top plots are for the training data, the middle ones for the validation data, and the below ones for the test data; showing that distribution of the training, validation and test datasets are almost the same, as they should be.

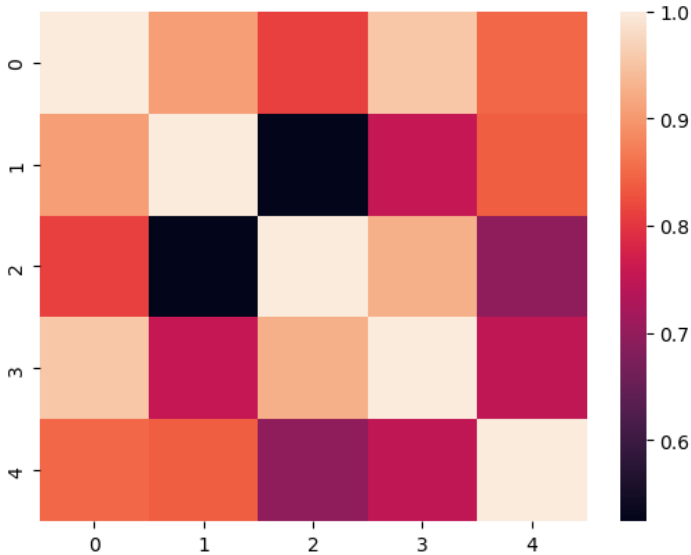


Figure 10. Correlation heat-map of the input data in the single-shot measurement scenario; due to high correlation between phase differences of BPM2 – BPM1, shown as 0, and BPM4 – BPM1, shown as 3, we can exclude the BPM4 – BPM1 phase difference data from our dataset to reduce dimensionality of the data; the signal from BPM4 is less reliable than it from BPM2 in the real data collected while commissioning on the machine in June, 2022

3.1.3 Data pre-processing

Four different types of errors are added to the perfect machine, noise-free, data. BPM longitudinal positions within the machine could be different from the designed values, potentially due to installation and construction limitations, resulting in BPM Δs error. Plus, the BPMs phase readouts may be erroneous, induced by electronic limitations. There are also errors arising from production limitations when fabricating the cavities. Such limitations could give rise to errors in both RF amplitude and phase gap-to-gap. The errors in the RF parameters and of the BPM longitudinal placement are "static", in that, once different elements of the machine are

installed, they will have a given reproducible value, as compared to the BPM readout errors, which will be random each time the diagnostic is used. All the errors are modelled as being normal distributed. The different types of errors and their 3 standard deviation values, which are the maximum theoretical values calculated in the technical design of the DTL1 tank, are summarized in Table 2. As the error values are considered as being maximum, the models are expected to outperform for the real data.

Error	Magnitude	Type
BPM $\Delta\varphi$	$\pm 1^\circ$	Dynamic
BPM Δs	$\pm 100 \mu\text{m}$	Static
RF ΔA	$\pm 0.2\%$	Static
RF $\Delta\varphi$	$\pm 0.5^\circ$	Static

Table 2. Different types of errors and their magnitudes, added to the noise-free Perfect Machine data; BPM $\Delta\varphi$: the BPMs phase readout error due to electronic limitations, BPM Δs : the error in BPM longitudinal positions due to installation and construction limitations, RF Amplitude and RF $\Delta\varphi$: errors in both RF amplitude and phase readouts; Static errors are the ones which have fixed reproducible magnitudes, while the dynamic one has different changing values in different times

The noise-added data then needs to be scaled into $[0,1]$ for the optimization algorithm to have a faster convergence. Since the labels in our data are of quite different scales, 54° for the RF phase, 1% for the RF amplitude and 0.02% for the input energy, they should be scaled to $[0,1]$ as well to get good initial weights, and to give all the outputs the chance to contribute equally to the network training.

3.2 ANN model weight initialization

Weight initialization is an important design choice when developing deep learning neural network models. To get output of activation functions of the links in every ANN layer being of order one using random walk theory, [26], the best initial values for the weights, ω , are random numbers of zero mean and $\frac{1}{k}$ variance, where k represents the number of inputs in the layer; while the best initial values of biases in the layer, b , are random numbers of zero mean and unit variance. That is, if the number of inputs to a hidden layer is, for example, 16, the best initial values for the weights are random numbers of zero mean and variance $\frac{1}{16}$, and the best initial values of the biases are random numbers of zero mean and zero variance.

3.3 ANN model weight scaling

Weight scaling is a technique that can help better predictions in some directions where there are many sample points whose corresponding target values are very similar, like the overlapped curves shown in Figure 6, [27]. By setting the scale of RF amplitude data in the target points being smaller than the scale of other target values, namely RF phase and input energy, we will force the corresponding weights in the RF amplitude being bigger by the same scale, making the models more flexible in the RF amplitude direction and the cost function get larger in that direction compared to other target directions. Different scaling factors were tested and the best one was 0.5, resulting in increasing the prediction accuracy in the RF amplitude by almost 100%, from 35 - 40% to 70 - 75%.

3.4 ANN model description

There are a wide variety of ML techniques that could have been used in this project. As a kick-off, having access to plenty of simulated data samples, AAN models, or more accurately, Deep Learning models could be a good option, for they give higher performances when big amount of data

is provided, compared to classical ML techniques such as SVM, Random Forest, Regression, and so on [28]. The more data we have, the deeper networks could be, resulting in more accurate models. Another reason why ANN models is a good option for this project is that they could be easily deployed in the control system at ESS using Field Programmable Gate Arrays (FPGAs) as a hardware module or via C++ APIs to develop software modules. The ML framework was chosen to be PyTorch to have the ease to use GPUs to run models faster.

A schematic of ANN model structures is shown in Figure 11. In this project, the number of inputs is 5, 10, and 15 for single-shot, double-shot, and triple-shot measurement scenarios, respectively. Excluding some of highly-correlated inputs, discussed in 3.1.2, the number of inputs reduced to 4, 8 and 12 for the mentioned measurement scenarios to reduce the dimensionality of input space, and to reduce risks of overfitting. The number of outputs is 3 for all the scenarios, which are RF phase, RF amplitude and input energy. The number of hidden layers determines how deep the network is, while the number of hidden nodes in each hidden layer specifies the width of the network. For the networks to capture the nonlinear behavior of data, deeper networks are preferred to wider ones [29] and [30].

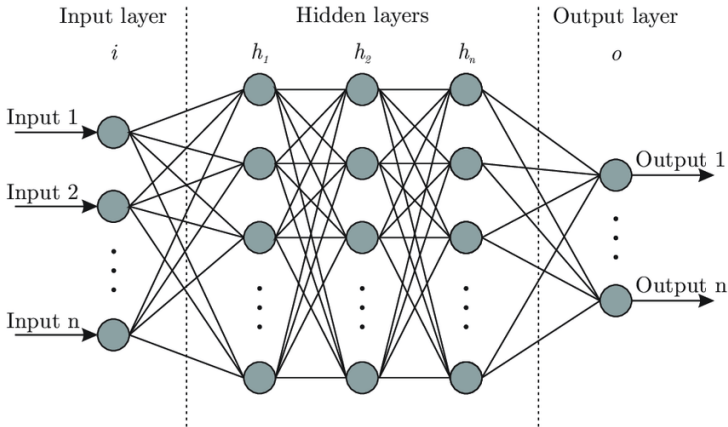
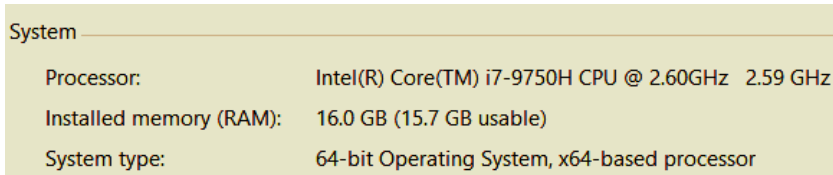


Figure 12. ANN model structures, [31]

The models developed were all fully-connected with different number of hidden layers and hidden nodes for different measurement scenarios, and it turned out that for the single-shot one, double-shot ones and the triple-shot one, at least 6, 5 and 4 hidden layers were needed, respectively. The number of hidden nodes in each hidden layers were chosen to be a power of 2, such as 8,16, and 32. Regarding the learning rate orders, it was realized soon that they should be small of order 10^{-3} or 10^{-4} . Decaying learning rates to take big steps at initial epochs and small steps at later epochs for the networks to converge better to the optimal weights was implemented. Different PyTorch built-in decaying learning rates functions were tested, but all my models faced reproducibility issues, which is common in ML, as discussed in [32]. A decaying learning rate technique was instead coded to start from $2 * 10^{-3}$ as the initial rate, reducing by a factor of 1.5 every 20 epochs. The ADAM optimization turned out to be the best and fastest one in comparison to the other ones such as Stochastic Gradient Descent (SGD) with momentum, RMSprop, and Mini Batch Stochastic Gradient Descent (MB-SGD). The activation function in the hidden layers is set as ReLU due to its non-zero gradients in positive arguments, and subsequently faster convergence for the networks compared to Sigmoid and Tanh. Both Mean Squared Error (MSE) and

Mean Absolute Error (MAE) loss functions, MSELoss and L1Loss in PyTorch, were tried out, and having a regression problem, the MSE one was chosen as the one. Different batch sizes of order 2 to the power of 5 to 10 meaning 32 to 1024, were tested, and 128 and 256 were proven to be the best ones. As there was no overfitting happening, there was no need for any regularization techniques, such as weight decaying or L2 regularization, L1 regularization, drop-out, or pruning. Since the networks are not so deep, there was no need to have Batch Normalization, BatchNorm2d in PyTorch, layers in the networks. The networks needed only 300 epochs to converge, so the trainings were fairly fast. It took me 1.5 hours, 3 hours, and 5 hours for the single-shot measurement, the double-shot ones, and the triple-shot one using a laptop with the specifications shown in Figure 13.

A screenshot of a system information window with a light green background. The title bar reads "System". Below the title bar, there are three rows of text: "Processor: Intel(R) Core(TM) i7-9750H CPU @ 2.60GHz 2.59 GHz", "Installed memory (RAM): 16.0 GB (15.7 GB usable)", and "System type: 64-bit Operating System, x64-based processor".

System	
Processor:	Intel(R) Core(TM) i7-9750H CPU @ 2.60GHz 2.59 GHz
Installed memory (RAM):	16.0 GB (15.7 GB usable)
System type:	64-bit Operating System, x64-based processor

Figure 13. Laptop specifications

To monitor how the training was happening and to figure out how well the models worked for each single output prediction over epochs, different techniques were tested. First, both the training and validation losses versus epochs were plotted, shown in Figure 14, to make sure the models were being trained well and there were no either overfitting or underfitting problems with the models. Both the training and validation MSE loss values when the networks were well-converged were in the order of 10^{-4} and 10^{-5} for the single-shot measurement and the rest, respectively. The spikes in the plot come from the fact that the errors are calculated based on the difference between the predictions and their corresponding target points in the last batch of the dataset, and not the

whole dataset, in each epoch; hence, the models might not be well fitted to those points, resulting in the spinks.

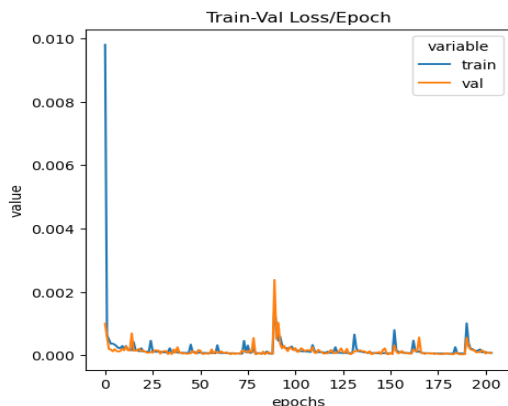


Figure 14. Training and validation losses versus epochs; Shows that the networks were being trained well and as there is not a big difference between the training and validation losses plots and the training loss is decreasing over epochs, so the networks do not either overfit or underfit to the data, respectively.

Another visualization that gave us a good view of how well the models were predicting different outputs was to plot the number of misprediction over epochs at a semi-logarithmic scale. By misprediction, it means the predictions that its difference with their corresponding target points is bigger than the requirements for each output. The reason why the number of mispredictions was needed to be at a logarithmic scale was for us to get a chance to explore more into small numbers of mispredictions, and to reflect the single number of misprediction onto the horizontal axis, for log of 1 is zero. In this way, the performance of the models was investigated for each output separately. An example of such plots is shown in Figure 15.

Number of mispredictions per epoch

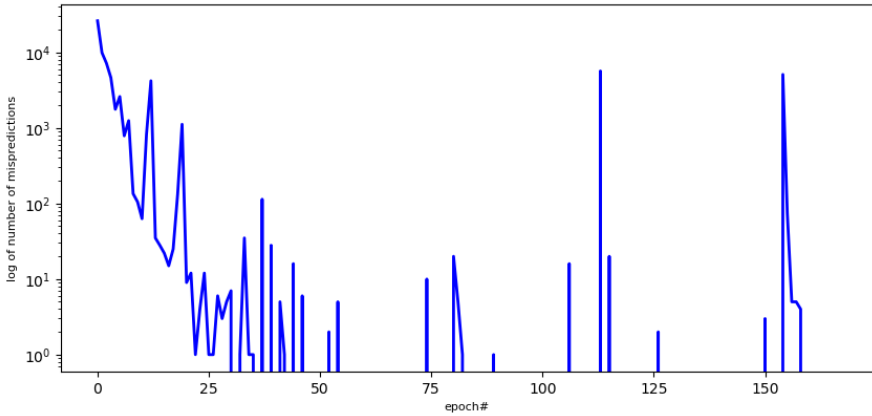


Figure 15. Number of mispredictions for RF amplitude during training on a logarithmic scale using double-shot measurement scenario; the plot shows the training is going well as the number of mispredictions decreases over epochs

As a more detailed investigation into the performance of the models during training, some animations of histograms of prediction errors for both scaled and original data for every output was made².

To get even higher performances, especially in RF amplitude, different built-in PyTorch ensembles using *torchensemble* package such as Fusion, Voting, Bagging, Gradient Boosting, Snapshot, and Fast Geometric ensembles, [33], were tested on the data. Despite the fact that they all took more time for training, they did not make any improvements with results compared to the models presented here.

² An example of such animations will be presented in the presentation.

4 Measurement scenarios and Results

In this chapter, first a description of all the histogram plots presented in the report is given in 4.1. Then, different measurement scenarios and their resulting results are presented. The single-shot measurement is the first one, which is discussed in 4.2. Then, two different double-shot measurement scenarios are implemented to see which one works better in a hope for any improvements with the prediction performance. They are presented in 4.3. Lastly, a triple-shot measurement scenario is tested to make the results even better, being presented in 4.4.

4.1 Description of histogram plots

The histograms plots and the relevant results correspond to training the networks using the full datasets, without excluding any of highly-correlated features from the datasets as discussed in 3.1.2. The reason why is that there were no significant differences between the performance of the models using full datasets or reduced datasets. In all the histogram plots presented, the left plots target the scaled data while the right ones correspond to the unscaled original data. The top ones are for the prediction error for the RF phase, the middle ones for the RF amplitude, and the below ones for the input energy, respectively. The yellow lines are the 3 standard deviation interval corresponding to 99.7% confidence of the prediction errors, the green ones are the 2 standard deviation interval corresponding to 95% confidence of the prediction errors, and the red ones show the requirements set by the ESS, so the yellow lines are desired to be between the red lines to show that the requirements are met by models. The black line represents the mean value of the prediction errors. The resulting values for the prediction error confidence interval, the requirements, and the mean values are presented in the legend of the plots. It is useful to mention that only the 3 standard confidence interval matters, not the 2 standard confidence interval, so the yellow lines should be inside

the red lines, not the green ones, to show that models are successful. The green lines are just to express the 95% confidence of the predictions for the RF amplitude to be within the requirements. It should be re-emphasized that the prediction accuracies are calculated based on the 99.7% confidence, not the 95% one.

The prediction accuracy is the metric expressing how well the predictions are compared to the requirements. They are calculated in a way that if a model fails to meet the requirements, meaning that the yellow lines are outside the red lines range, they get values less than 100%; and the smaller values they have, the further from the requirements the model performs. If the model prediction errors are exactly the same as the requirements, the prediction accuracy is exactly 100%, and if they outperform the requirements, meaning that the yellow lines are between the red line, the predictions accuracy takes values more than 100%, and the lower prediction errors by the models are obtained, the larger values this metric represents. The formula of the prediction accuracy is defined as below:

$$\text{prediction accuracy (\%)} = 100 * \frac{\text{Required error prediction bound}}{3 \text{ standard deviation confidence interval mean bound}}$$

where the denominator is the average of the upper bound and the lower bound of the 3 standard deviation confidence intervals.

There is some performance leakage from the scaled data, which the models are trained and validated based on, to the original unscaled data, which are the base to evaluate the models. That can be seen from lower prediction accuracies in right plots compared to them in the right plots in all the histogram plots. The possible reason behind that could be that noise-signal ratio of the data in the outputs is high, especially in RF amplitude. Adding big noise levels could change the distribution of data, so transforming back the scaled data to the original ranges of them could result in some outputs which are slightly different from the targets; hence

the prediction error values using the scaled data could be different from them using the transformed-back data. Such performance reduction in input energy is big compared to the other outputs because the range of input energy data is $[0.99, 1.01]$, while the acceptable noise level considered for the input energy to be added to the noise-free data is 0.04%. The performance reduction for the other outputs is rather negligible. It is useful to mention that the prediction accuracies of the scaled and transformed-back data if no noise is added are exactly the same, proving the effect of the additive noise on the performance leakage.

4.2 Single-shot measurement scenario

In the first attempt, single-shot measurement scenario, discussed in section 2.7, is implemented, in which the model designed is tested on the BPMs data in a real-time manner; that is, every time the set-points of the machine get tuned, the resulting BPMs data are read out and their phase differences are calculated to be used as a test point at that time. The number of samples in the dataset for this scenario is 363000, and the dataset is divided into training, validation and test datasets by a factor of 80%, 10% and 10%, respectively.

The dataset structure needed here should have the phase difference values of every BPM compared to the first BPM, BPM 1, as the input, creating a 4-dimensional feature space due to excluding the data of BPM4 – BPM1 thanks to its high correlation with the data of BPM2 – BPM1, and their corresponding RF phase and amplitude, and input energy, φ , A, E, respectively, as the labels. In Figure 16, the histogram of the prediction error of single-shot measurement using the best model, whose specifications are tabulated in Table 3, is shown.

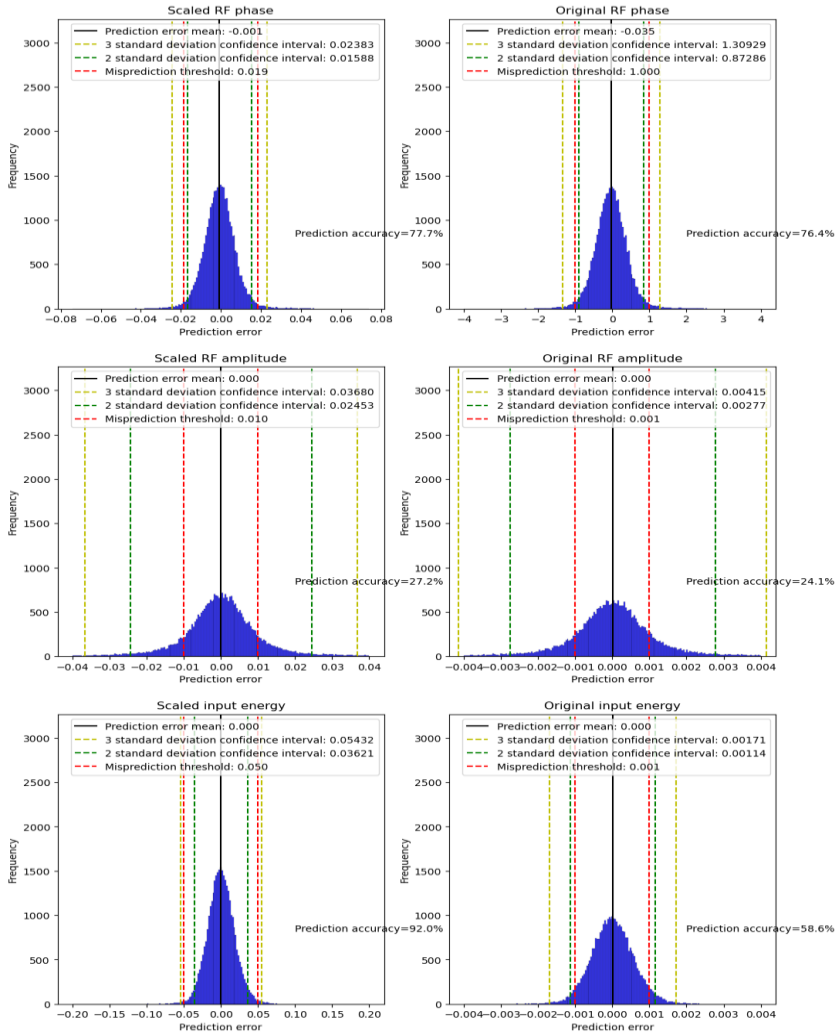


Figure 16. Histogram of the prediction error of single-shot measurement using the best model. The plot description is presented in 4.1. The best model here fails at fulfilling the requirements (red lines) for all the outputs by 95% confidence (green lines) or 99.5% confidence (green lines), proving that the single-shot measurement scenario does not work well here. The left plots show histograms of prediction errors for the original data, while the left ones are for the scaled data.

Layer widths	16-32-16-16-16-8
Initial LR	2e-3
Batch size	256
Optimization algorithm	ADAM
Number of epochs	300
Loss function	MSE loss
Activation function	ReLU

Table 3. Model structure and hyperparameter values for the best model in the single-shot measurement scenario

4.3 Double-shot measurement scenarios

In this section, the double-shot measurement scenario is presented. That is, the BPMs data related to the first shot are read out and their phase differences are calculated and considered as values for the initial 5 features of the data points, while there needs to take one more shot of measurement either through shifting the RF phase by certain degrees, discussed in 2.1.1.1, or via shifting the RF amplitude by certain percentages, discussed in 2.1.1.2. Since it is complicated to tune the input energy precisely, the second shot could not be taken in the input energy direction. The number of samples in the dataset for this scenario is twice it in the single-shot one, due to considering both positive and negative shifts, so in total it is 726000, and the dataset is divided into training, validation and test datasets by a factor of 80%, 10% and 10%, respectively. The number of features are 10 consisting of 5 BPM pair differences in the first shot, and 5 BPM pair phase differences after taking the shifts.

The shifts have to be only positive for the data points whose values of their corresponding labels exceed the lower limits by applying the shift, and only negative for the data points whose values of their corresponding labels exceed the upper limits by applying the shift; otherwise, they could be and should be both negative and positive to cover all the possible shifts while tuning the machine in reality. The datasets created for training the

models should be smart in that way. The best model order for both the double-shot measurement scenarios is 16-32-16-16-8. The hyperparameter values are the same as in the single-shot one.

4.3.1 In RF phase direction

Looking at the upper plot in Figure 6, we can see that some curves are partly flat in the RF phase direction, so the shift in this direction should be big enough to make the second shot sufficiently different from the first one, but not too big in a way that it becomes hard for the real process to get tuned and at the same time, to stay stable. This measurement scenario is depicted in Figure 17. Different phase shifts were tested and the best value was realized as 25 degrees. Table 4 depicts different values for the RF phase shift and their resulting prediction accuracies. Histogram of the prediction error using the best model for this measurement scenario is illustrated in Figure 18.

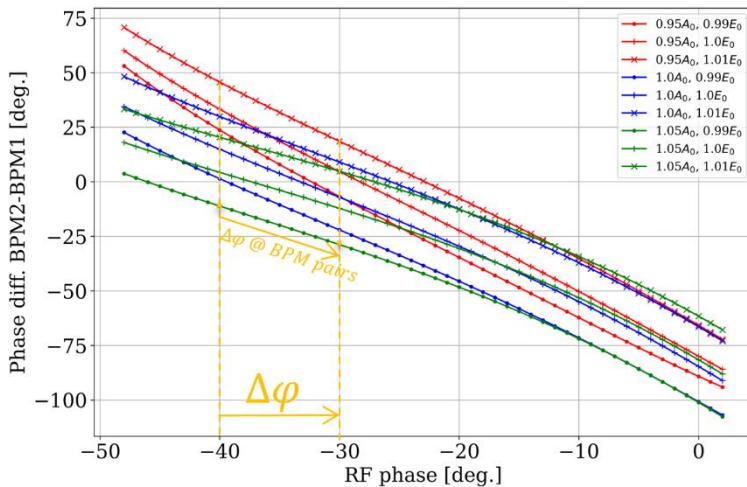


Figure 17. Double-shot measurement scenario in the RF phase direction

Phase shift (Degrees)	RF phase (φ), Scaled (%)	RF phase (φ), Original (%)	RF phase (A), Scaled (%)	RF phase (A), Original (%)	Input energy (E), Scaled (%)	Input energy (E), Original (%)
3	103.1	103	34	31	137	93
5	107	106.9	40.3	36.8	150	101.4
10	128	127.7	50.8	46.4	176	119
15	140	139.5	57.9	52.9	191.7	130
20	145.2	145	65.8	60.2	196	132.5
25	161.3	161	78.8	72	207	140

Table 4. Prediction accuracies for different RF phase shifts; the best RF phase shift and its corresponding prediction accuracies are bold. As the RF phase shift gets bigger, the prediction accuracies increase, which is sensible, for the much further the second shot is taken, the chance to avoid the data confusion, discussed in 4.2, gets higher. Form practical point of view at ESS, it is applicable to implement the RF phase shift by 25 degrees while tuning the machine by taking small steps.

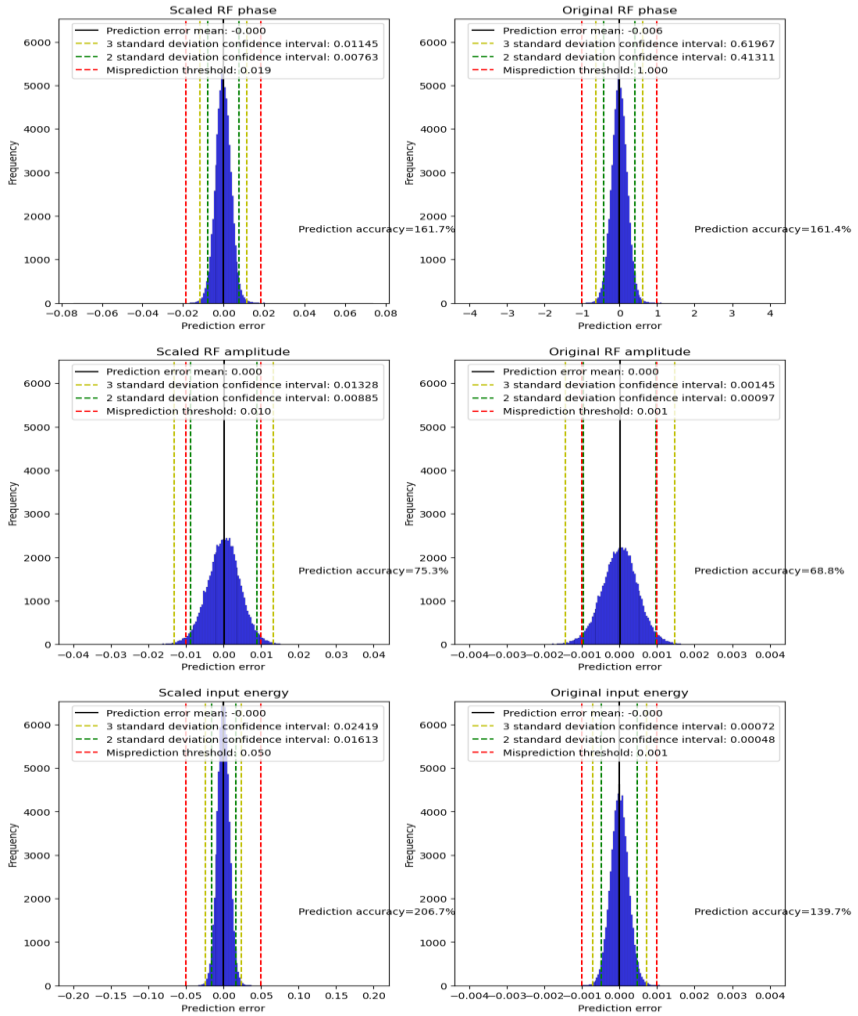


Figure 18. Histogram of the prediction error using the best model for the double-shot measurement scenario in the RF phase direction. The plot description is presented in 4.1. The best model meets the requirements (red lines) for the RF phase and input energy, but not for the RF amplitude by 99.7% confidence (yellow lines). The reason is discussed in 2.6. However, it fulfills the requirement in RF amplitude by 95% confidence (green lines). The 99.7% confident prediction accuracies showing the performance of the model are 161%, 68%, and 140% in RF phase, RF amplitude and input energy, respectively.

4.3.2 In RF amplitude direction

Considering the plot (b) in Figure 6, we can see that some curves are not quite separate and thus identifiable in RF amplitude direction; thus, it might be a good idea to take the second shot in the RF amplitude direction, instead of the RF phase direction. Again the shift should be big enough to make the second shot sufficiently different from the first shot, but not too big. This measurement scenario is depicted in Figure 19. Table 5 presents the prediction accuracies using the best models for different RF amplitude shifts. Histogram of the prediction error using the best model for this measurement scenario is illustrated in Figure 20.

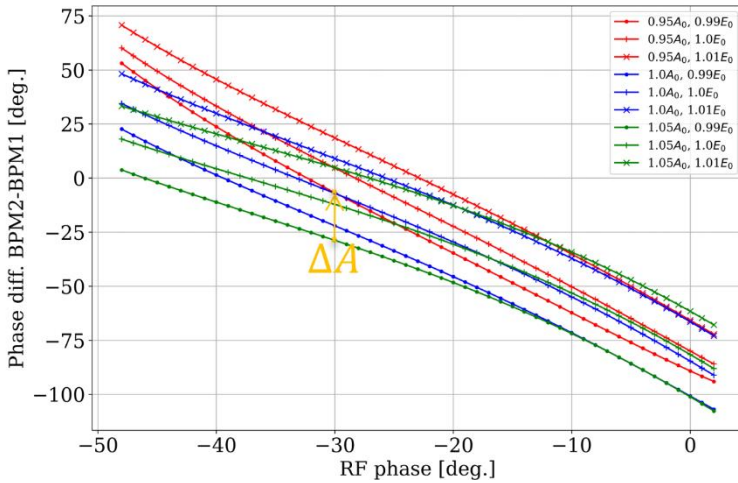


Figure 19. Double-shot measurement scenario in the RF amplitude direction

Amplitude shift (%)	RF phase (φ), Scaled (%)	RF phase (φ), Original (%)	RF phase (A), Scaled (%)	RF phase (A), Original (%)	Input energy (E), Scaled (%)	Input energy (E), Original (%)
2	113.7	113.5	36	33	155.8	105.3
4	114.5	114.2	35	32	151.5	102.4
6	116.5	116.3	35.4	32.2	154.7	104.7
8	117.2	117.1	35.8	32.8	154.6	104.9
10	118.6	118.4	36.2	33.5	156.1	106.2

Table 5. Prediction accuracies using the best models for different RF amplitude shifts; the best shift and its corresponding prediction accuracies are bold. It should be noted that taking the second shot of measurement having different RF amplitude shift values do not affect the prediction accuracies significantly, so the smallest RF amplitude shift which is the easiest and fastest one to put in the control system is chosen as the best one. In addition, this measurement scenario underperforms the double-shot one in the RF phase direction significantly, presented in 4.3.1, so this scenario is disregarded.

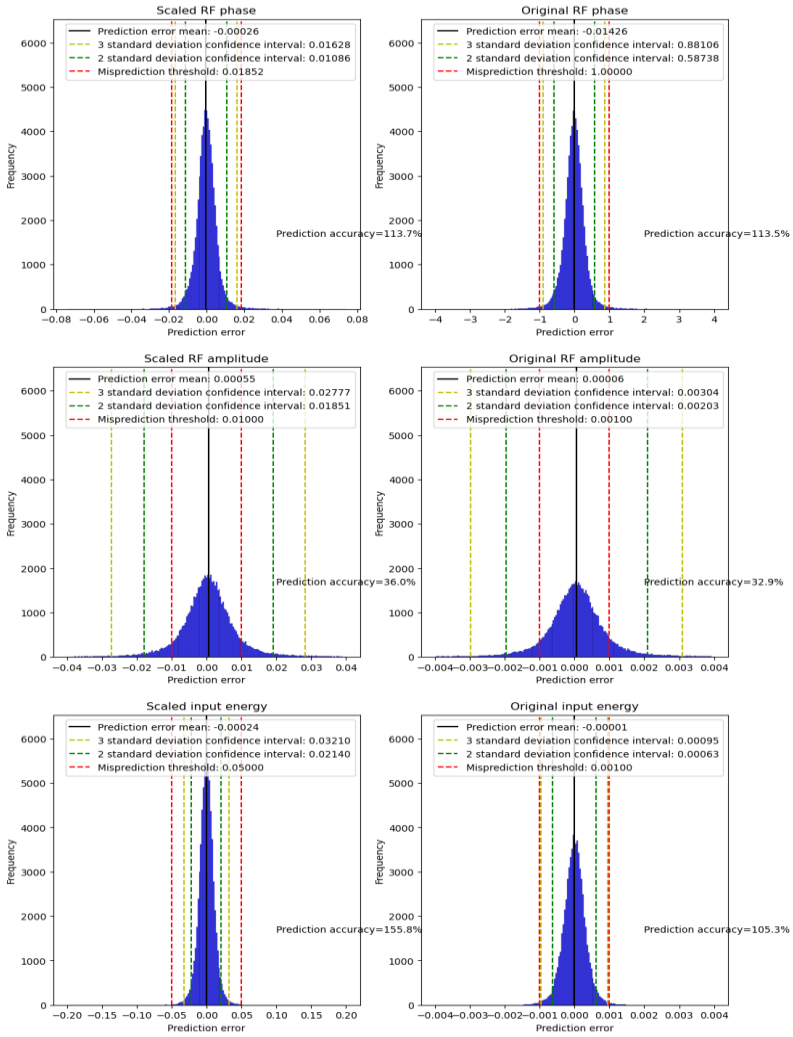


Figure 20. Histogram of the prediction error using the best model for the doubleshot measurement scenario in RF amplitude direction. The best model meets the requirements (red lines) for the RF phase and input energy, but not for the RF amplitude. The 99.7% confident prediction accuracies showing the performance of the model are 113%, 33%, and 105% in RF phase, RF amplitude and input energy, respectively. This double-shot scenario underperforms the double-shot scenario in RF phase, presented in 4.3.1, but outperforms the single-shot one, presented in 4.2.

4.4 Triple-shot measurement scenario

Since the predictions in the RF amplitude direction are not good enough yet, the prediction error for the RF amplitude is still bigger than the requirement by 1%, a third shot of measurement might help. The idea comes from the fact that although some curves overlap, they have different slopes at the overlapping regions. The slopes are defined by the triple-shot measurement scenario in that the second shot is taken via a shift in the RF phase direction relative to the first shot, which is horizontal and is shown by light orange arrow, and the third one is taken via the shift in the RF amplitude direction relative to the second shot, which is vertical and is shown by dark orange arrow. The idea is depicted in Figure 21. The resulting measurement is shown as the brown arrow in the figure.

The dataset created should be smart in a way that it covers both negative and positive shifts both in the RF phase and amplitude directions, but should not cross the upper and lower limits while taking the shifts. The number of samples in the dataset for this scenario is 4 times it in the single-shot one, due to considering both positive and negative shifts in the RF phase and both positive and negative shifts in the RF amplitude, so in total it is 1452000, and the dataset is divided into training, validation and test datasets by a factor of 80%, 10% and 10%, respectively. The number of features is 15 consisting of 5 BPM pair differences in the first shot, 5 BPM pair phase differences after taking the RF phase shifts in the second shot, and 5 BPM pair phase differences after taking the RF amplitude shifts in the third shot. The best model order for the triple-shot measurement scenario is 16-32-16-8. The hyperparameter values are the same as in the single-shot one. Table 6 presents prediction accuracies using this model for different RF phase and amplitude shifts. Histogram of the prediction error using this model for this measurement scenario is illustrated in Figure 22.

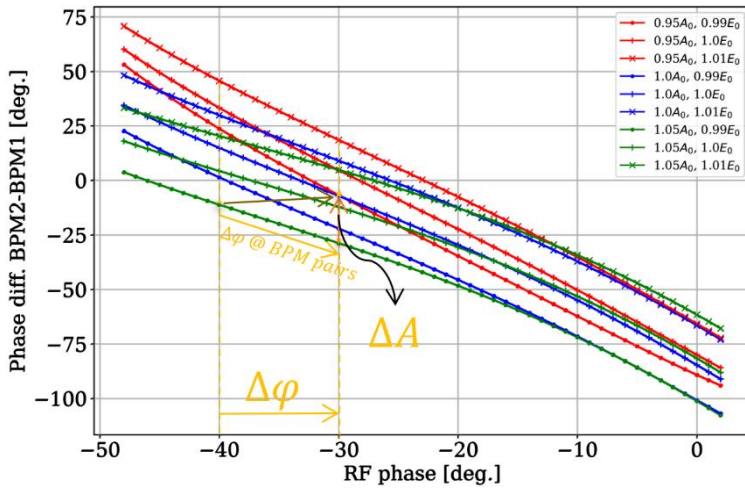


Figure 21. Triple-shot measurement scenario; light orange arrow: the second shot in RF phase direction, the dark orange arrow: the third shot in RF amplitude direction, and the brown arrow: resulting triple-shot measurement.

Amplitude shift (%)	Phase shift (Degrees)	RF phase (φ), Scale d (%)	RF phase (φ), Original (%)	RF phase (A), Scaled (%)	RF phase (A), Original (%)	Input energy (E), Scaled (%)	Input energy (E), Original (%)
2	3	110	110	34.2	31.2	152.4	103.2
2	5	110	110	37.2	34	146.9	99.3
2	10	121.4	121.2	26.9	42.8	171.2	115.7
2	15	170.6	170.2	68.9	62.9	231	156.1
2	20	186.4	185.9	83.2	76	251.4	170
4	3	101	101	31.6	28.8	143	96
4	5	101.5	101.1	32.1	29.2	140.1	94.2
4	10	112.7	112.5	31.9	29.2	140.4	95
4	15	125	125	50	45	173	117
4	20	130	130	55.5	50	184	124
6	3	102.9	102.6	34.1	31.1	139	94
6	5	99	98.8	31.4	28.6	135.1	91.3
6	10	128.7	128.4	51.8	42.3	176.8	119.53
6	15	133.6	133.3	53.2	48.6	178.8	121
6	20	163.2	162.1	64.2	59.2	212.3	139.1
8	3	113.4	113.2	34.8	31.8	153.6	103.9
8	5	114.2	113.8	36.3	33.2	158.3	106.1
8	10	142.4	141.5	59.1	57.1	189.3	123.3
8	15	158.1	157.7	66.23	60.5	214.2	144.8
8	20	159.7	159.4	62.41	59.25	222.8	153.5
10	3	112.6	112.4	35.5	32.5	151.4	102.3
10	5	114.3	113.8	37.2	33.2	152.5	102.2
10	10	98.7	98.5	39.8	36.3	134.3	90.7
10	15	125.1	124.9	52.7	48.1	171.2	115.7
10	20	132	131.6	56.7	51.8	182.5	123.3

Table 6. Prediction accuracies using the best models for different RF phase and amplitude shifts; the best RF phase and RF amplitude shifts and the corresponding prediction accuracies are bold. As the RF phase shift gets bigger and the RF amplitude shift be small, the prediction accuracies are higher, which is what we got in the double-shot measurement scenarios, discussed in 4.3. Form a practical point of view at ESS, it is applicable to implement the RF phase shift by 25 degrees while tuning the machine.

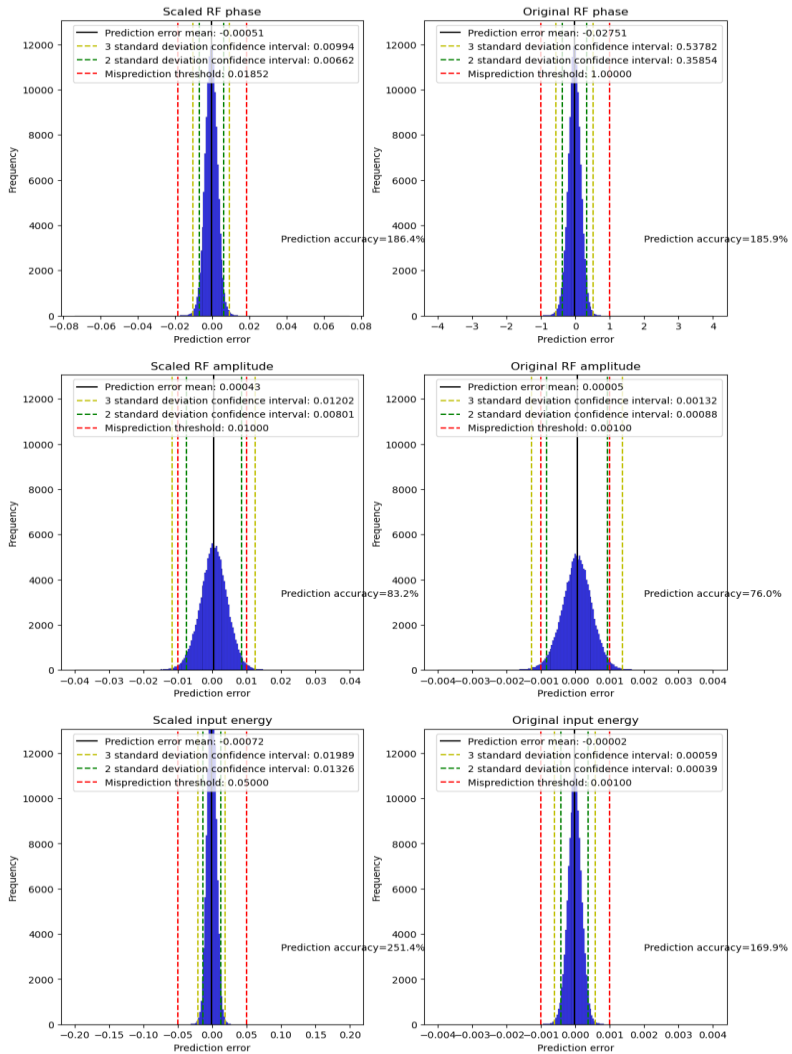


Figure 22. Histogram of the prediction error for the triple-shot measurement scenario. It is the best measurement scenario, and the best model meets the requirements (red lines) for the RF phase and input energy, but not for the RF amplitude by 99.7% confidence (yellow lines). However, it fulfills the requirement in RF amplitude by 95% confidence (green lines). The 99.7% confident prediction accuracies showing the performance of the model are 186%, 76%, and 170% in RF phase, RF amplitude and input energy, respectively.

As a summary, the results using the best models for different measurement scenarios are presented in Table 7. The results are compared with the previous master's thesis results in which only the single-shot measurement scenario was implemented, [4], and the requirements. As discussed in 2.7, since the nature of the data is a non-function mapping between the inputs and the outputs, the single-shot measurement should not suffice to get good results, which is reflected in Table 7. As an idea, multi-shot measurements could solve the challenge by defining new features in the feature space, making the similar inputs different and resulting in function mapping between the inputs and the outputs. As a natural option, a double-shot measurement in either the RF phase or the RF amplitude direction, but not in the input energy as discussed in 4.3, could be one of them. According to Natlalia Milas, as my supervisor, it is easier to change the RF phase rather than the RF amplitude in the LLRF system; hence, the first double-shot measurement would be in the RF phase direction, giving very good results as presented in Table 7. As the predictions in the RF amplitude have yet to improve, the second double-shot measurement option could be in the RF amplitude direction, though it is harder in practice to perform, outperforming the single-shot one and the requirements in the RF phase and input energy, but underperforming the double-shot one in the RF phase. As the last effort, the triple-shot measurement scenario was tested, giving the best results compared to all the other ones. Using weight scaling technique, discussed in 3.3, better predictions could be made for the RF amplitude for all the measurement scenarios. As discussed in 2.6, the reason why none of the models succeeds in meeting the requirements for the RF amplitude prediction is the fundamental limitation in its data.

Error distributions	$3\sigma_{\varphi}[\text{degrees}]$	$3\sigma_A[\%]$	$3\sigma_E[\%]$	$\mu_{\varphi}[\text{degrees}]$	$\mu_A[\%]$	$\mu_E[\%]$
Requirements	1	1	0.1	0	0	0
Previous project	2.242	1.535	0.421	-0.049	-0.007	0.011
Single-shot	1.31	4.15	0.117	-0.035	0	0
DS in RF Phase	0.62	1.45	0.072	-0.006	0	0
DS in RF Amplitude	0.88	3	0.095	-0.0146	0	0
Triple-shot	0.53	1.32	0.06	-0.027	0	0

Table 7. Results of the best models using different measurement scenarios in comparison with the requirements and the previous master's thesis results, [4]; DS stands for Double-shot. φ , A , and E stand for the RF phase, RF amplitude, and input energy, respectively. 3σ and μ represent the 3 standard deviation confidence interval and the mean value of prediction errors, respectively. All the models, except the single-shot one, outperform the model in the previous master's thesis. The best model is the triple-shot one, and the second best one is the double-shot one in RF phase direction, which could be deployed in the control system at ESS to do RF phasing and monitoring, respectively, as discussed in 2.10.

5 Discussion and future work

As discussed in 4.2, it was expected that, regardless of any model structures, the single-shot measurement scenario does not yield satisfying results. That was resulted in the previous master's thesis, [4], where only this scenario was implemented. Hence, two double-shot measurement scenarios in the RF phase and RF amplitudes are implemented in this project, resulting in significantly better results than the single-shot one. The models also meet the requirements for the RF phase and the cavity input energy, but still not for the RF amplitude of being 99.7% confident which is statistically accepted, as discussed in 2.6. To get even better predictions, the triple-shot measurement is implemented and tested, giving the best results as expected. The RF amplitude predictions, however, are of 95% confidence using the double-shot measurement in the RF phase and the triple-shot one; thus, the beam physicists at the ESS should account for some small number of uncertainties for the RF amplitude predictions when tuning the machine. However, for monitoring and verification of the process within the machine, they can use the models without any uncertainty.

Another important aspect of the results are really accurate predictions for the cavity input energy, having less than 0.1% prediction error, showing that the models are more than 99.9% accurate on the input energy. Hence, being impossible to have any instrumentation to measure the cavity input energy in the ESS DTL section and the upstream sections, the models presented here could be to a good extent used as the virtual diagnostics (sensors) to monitor the input energy for daily use. That is so important to the ESS staff because it is the physical property that needs to be known in each cavity for them to keep track of the beam properly.

In addition to the better results, another merit of the presented models compared to the ones developed in the previous master's thesis is the sizes of the networks, which are extremely smaller. The model order of the single-shot, double-shot and the triple-shot models are only 16-32-16-16-

16-8, 16-32-16-16-8 and 16-32-16-8, respectively, in comparison with 160-160-80-80-40-40-80-80-160-160 in the previous master's thesis, which is seriously large and impractical. Another advantage is the fast convergence of the networks, taking only 300 epochs, in comparison with 20000 epochs in the previous master's thesis. One of the reasons why the presented models outperform the ones in the previous master's thesis is that better data handling and data pre-processing, and proper data scaling have been done in this project. Another reason is that all the 15 BPM pair phase differences, shown in Figure 8, are considered as the inputs in the datasets in the previous master's thesis, while as discussed in 2.7, 10 BPM pair phase differences have high correlation with the rest, so they should be excluded from the dataset.

As stated before, it is vital to work with models which meet the design requirements to do RF tuning. As the triple-shot one is the closest one to that among the other, this is the one which is going to be deployed to perform RF tuning of the DTL 1 tank; while since there is no serious need for very accurate models for the monitoring and verification, as discussed in 2.10, the double-shot one in the RF phase is the proper model in such a case. The reason why we would go with the double-shot one and not the triple-shot one in such cases is that the ESS staff need to wait until only the second shot of measurement is taken for the model to do the predictions, which is faster than the situation when they need to wait for the third shot as well.

Since the prediction accuracies of both the double-shot in the RF phase and the triple-shot models increase as the RF phase shift increases, there could be some limitations making the use of the best models in practice, though it is possible to imply big RF phase shifts by taking small steps to cover the shift range. As another limitation, the distribution of real data could be different from the data used for the project, even considering the added noise, causing the models to fail to make good predictions. As an idea for the future work, the models could get calibrated with the real data using transfer learning technique, [27], to update the weights in the last or two last hidden layers to get more fitted to the real data, and then use the calibrated model. If the size of real data is small, a part of it can get added

to the available simulated data to create big training and validation datasets, while the rest of the real data is considered as the only data in the test dataset, as some other future work. That would make the distribution of the training and validation dataset closer to the test dataset.

There are some other types of ML techniques that could be used in line with or complementary to this project in the future. ANN models are too confident about their predictions, while Bayesian Neural Networks (BNN), which can introduce the uncertainties from the model and provide the distributions over the weights and outputs instead of fixed certain weights [34], or Gaussian Process Regression (GPR), which can make predictions incorporating prior knowledge (kernels) and provide uncertainty measures over predictions [35], could be developed to get both the expected value and the variance of the predictions.

6 Conclusion

The project aims at developing ANN-based models to meet the requirements on the tuning parameters of the ESS DTL1 tank. The models are supposed to be deployed in the control system at ESS to be used either as a modeling or a monitoring and verification tool of the DTL process while starting up or ramping up the machine. As the requirements are really high, asking for model accuracies by 99%, there was a big challenge to reach such accuracies, especially when some noise, described in 3.1.3, is added to the simulated data to make the models robust against possible different distributions of real data compared to the simulated data, as discussed in 3.1.1. Deep learning models could be a good option, since the size of available data is large. The data consists of the BPM pairs phase differences as the inputs, and the RF phase, RF amplitude and input energy as the outputs, being simulated using OpenXAL and some noise, presented in 3.1.3, added to make the models robust. Different measurement scenarios were implemented and tested, and the resulting double-shot and triple-shot models meet all the requirements, except the RF amplitude which was discussed in 2.6. They also outperform the models developed in the previous master's thesis, [4], in all the predictions significantly. As mentioned in 2.8, though a lot of ML-based research has been done in the world of particle accelerators, just a few have been eventually used routinely as part of an accelerator's main control system; hence, there is a huge possibility to build more advanced intelligent accelerators benefiting from the AI and ML achievements, and we are happy to take such a step through this project.

7 Bibliography

- [1] M. Åberg, ESS Technical Design Report, European Spallation Source, 2013.
- [2] J. Galambos, "XAL Application Programming Structure," Knoxville, 2005.
- [3] T. Wangler, RF Linear Accelerators, John Wiley & Sons, Ltd, 2008.
- [4] J. Lundquist, "Tuning of the ESS Drift Tube Linac using Machine Learning," 2022.
- [5] R. Garoby, "The European Spallation Source Design," Physica Scripta, 2017.
- [6] [Online]. Available: https://en.wikipedia.org/wiki/File:ESS_Accelerator_tunnel_211_221.jpg.
- [7] [Online]. Available: https://www.researchgate.net/figure/The-schematic-representation-is-of-a-Drift-Tube-LINAC-where-ions-are-accelerated-using_fig1_235029687#:~:text=Figure%20-,The%20schematic%20representation%20is%20of%20a%20Drift%20Tube%20LINAC%20where,electric%20fields%2.
- [8] "INFN," [Online]. Available: <https://home.infn.it/en/media-outreach/infn->

newsletter/newsletter-focus/4972-sweden-european-spallation-source-linear-accelerator-grows.

- [9] "ESS," [Online]. Available: <https://europenspallationsource.se/article/2022/03/21/conditioning-first-drift-tube-linac-starts-ess>.
- [10] S. Ikegami, "Tuning of RF amplitude and phase for the drift tube linac in J-PARC," *Chinese Physics*, p. 577–582, July 2009.
- [11] T. Owens, "Phase scan signature matching for linac tuning," *Particle Acceleration*, p. 169–179, 1994.
- [12] H. T. Higo, "Some applications of ai to the problems of accelerator," *Proc.*, p. 701, 1986.
- [13] D. Weygand, "Artificial intelligence and accelerator control," *Brookhaven National Lab*, 1987.
- [14] E. Campbell, "Hybrid neural networks and their application to particle accelerator control," *International Society for Optics and Photonics*, p. 132–143, 1999.
- [15] C. J.A. Howell, "Control of a negative-ion accelerator source using neural networks," *Nuclear Instruments and Methods in Physics Research Section A: Accelerators, Spectrometers, Detectors*, p. 517–522, 1990.
- [16] P. W.C. Mead, "Optimization and control of a small-angle negative ion source using an online adaptive controller based on the connectionist normalized local spline neural network," *Beam Interactions with Materials and Atoms* 72, p. 271–289, 1992.

- [17] S. W.C. Mead, "Adaptive optimization and control using neural networks," *Nuclear Instruments and Methods in Physics Research Section A: Accelerators, Spectrometers, Detectors and Associated Equipment* 352, p. 309–315, 1994.
- [18] E. Friedman, Neural network technique for orbit correction in accelerators/storage rings, AIP Conference Proceedings, 1994.
- [19] K. K.H. Kim, "Simulation of the global orbit feedback system for pohang light source," *Proceedings of the European Particle*, p. 1906–1908, 2000.
- [20] E. N.R. Jennings, "Using archon to develop real-world dai applications," *IEEE expert* 11, p. 64–70, 1996.
- [21] R. W. Klein, "Developing a general purpose intelligent control system for particle accelerators," *Journal of Intelligent & Fuzzy Systems* 7, p. 1–12, 1999.
- [22] C. Emma, "Machine learning-based longitudinal phase space prediction of particle accelerators," *Phys. Rev. Accel. Beams* 21, p. 112802, Nov 2018.
- [23] X. Pang, "Advances in Proton Linac Online Modeling," *6th International Particle Accelerator Conference*, p. 1, 2015.
- [24] A. Larasati, "The relationship between data skewness and accuracy of Artificial Neural Network predictive model," *IOP Conf. Ser.: Mater. Sci. Eng.* 523, p. 012070, 2019.
- [25] R. Sakia, "The Box-Cox Transformation Technique: A Review," *Journal of the Royal Statistical Society*, pp. 169-178, 1992.

- [26] D. Sussillo, "Random Walk Initialization for Training Very Deep Feedforward Networks," *Neural and Evolutionary Computing*, Feb 2015.
- [27] J. Brownlee, 25 August 2020. [Online]. Available: <https://machinelearningmastery.com/how-to-improve-neural-network-stability-and-modeling-performance-with-data-scaling/>.
- [28] S. Mahapatra, March 2018. [Online]. Available: <https://towardsdatascience.com/why-deep-learning-is-needed-over-traditional-machine-learning-1b6a99177063>.
- [29] T. Nguyen, "Do wide and deep networks learn the same things?," *ICLR*, 2021.
- [30] B. Antognini, 2016. [Online]. Available: <https://stats.stackexchange.com/questions/222883/why-are-neural-networks-becoming-deeper-but-not-wider>.
- [31] M. Z. Dossett, "https://mindy-dossett.com/," 24 Jan 2021. [Online]. Available: <https://mindy-dossett.com/2021/01/24/intro-to-NN/>.
- [32] S. Bhojanapalli, "On the Reproducibility of Neural Network Predictions," 2021.
- [33] "Torchensemble," [Online]. Available: <https://github.com/TorchEnsemble-Community/Ensemble-Pytorch>.
- [34] J. W., "Training Bayesian Neural Networks, A study of improvements to training algorithms," Lund, 2020.

- [35] C. Rasmussen, *Gaussian Processes for Machine Learning*, The MIT Press, 2006.
- [36] E. Nilsson, "Internal Communication, ESS".
- [37] A. Edelen, "Neural Networks for Modeling and Control of Particle Accelerators," *IEEE Transactions on Nuclear Science* 63, pp. 878-897, Apr 2016.
- [38] "Open XAL," 2003. [Online]. Available: <http://openxal.github.io/>.
- [39] J. Brownlee, 2017. [Online]. Available: <https://machinelearningmastery.com/transfer-learning-for-deep-learning/>.

Lund University Department of Automatic Control Box 118 SE-221 00 Lund Sweden	<i>Document name</i> MASTER'S THESIS	
	<i>Date of issue</i> November 2023	
	<i>Document Number</i> TFRT-6193	
<i>Author(s)</i> Amin Hosseini Nejad	<i>Supervisor</i> Karin Rathsmann, ESS Natalia Milas, ESS Bo Bernhardsson, Dept. of Automatic Control, Lund University, Sweden Johan Grönqvist, Dept. of Automatic Control, Lund University, Sweden Anders J Johansson, Dept. of Electrical and Information Technology, Lund University, Sweden (examiner)	
<i>Title and subtitle</i> Developing an ML-based model for RF tuning of the DTL machine at ESS		
<i>Abstract</i> <p>The European Spallation Source (ESS) infrastructure is being constructed in Lund, and will be one of the most powerful research facilities of its type in the world. The ESS linear accelerator (linac) utilizes different accelerating sections where a wide variety of techniques should be employed to accelerate a beam of protons to 2 GeV kinetic energy through Radio Frequency (RF) cavities before being collided with a tungsten target for the final production of neutrons, through the process of spallation.</p> <p>This master's thesis is a continuation on another master's thesis project, (Lundquist, 2022), in which the focus was more on particle accelerator physics and to introduce some ML models using single-shot measurement scenario, which all failed to meet the requirements. This thesis, however, is focused on developing more ANN- models for both single-shot and multi-shot measurement scenarios, which succeed in meeting the requirements. Another focus of the project is to make the models small and feasible to be deployed in the ESS control system. The data is the simulated response of the Beam Position Monitor (BPM) sensors for the first Drift Tube Linas (DTL) tank, DTL1, at EES. DTL tanks are of great importance due to their influence on the overall performance. This will give the ESS physicists a powerful tool to direct the proton beam within the whole set of the DTL tanks properly, leading to a better control and thus, fewer beam losses once they start with the power ramp-up of the linac. The deployment of ML-based models in the ESS control system will be a step towards more automated and intelligent particle accelerators in this infrastructure and in similar future facilities.</p>		
<i>Keywords</i>		
<i>Classification system and/or index terms (if any)</i>		
<i>Supplementary bibliographical information</i>		
<i>ISSN and key title</i> 0280-5316		<i>ISBN</i>
<i>Language</i> English	<i>Number of pages</i> 1-65	<i>Recipient's notes</i>
<i>Security classification</i>		

<http://www.control.lth.se/publications/>